

An asymptotic stability proof and a port-Hamiltonian physics-informed neural network approach to chaotic synchronization

Behnam Babaeian^a, Marius E. Yamakou^a

^a*Department of Data Science, Friedrich-Alexander-Universität Erlangen-Nürnberg, Nürnberger Str. 74, 91052 Erlangen, Germany*

Abstract

We study chaotic synchronization in a five-dimensional Hindmarsh–Rose neuron model augmented with electromagnetic induction and a switchable memristive autapse. For two diffusively coupled neurons, we derive the linearized error dynamics and prove global asymptotic stability of the synchronization manifold using a quadratic Lyapunov function. Verifiable sufficient conditions follow from Sylvester’s criterion, and convergence is established using Barbalat’s lemma. A Helmholtz decomposition splits the error field into conservative and dissipative parts, yielding a closed-form synchronization energy and its dissipation law, which quantify the energetic cost of synchrony. Numerical simulations confirm complete synchronization, monotone decay of the synchronization energy, and close agreement between Lyapunov and Hamiltonian diagnostics across parameter sweeps. Building on these results, we introduce a port-Hamiltonian physics-informed neural network that embeds the conservative/dissipative structure through tailored losses and structural priors. The learned Hamiltonian and energy-rate match analytical benchmarks, providing an energy-aware, data-driven template for modeling and control of nonlinear neuronal synchronization.

Keywords: biological neurons, synchronization, Lyapunov function, synchronization energy, Hamilton function, physics-informed neural networks, port-Hamiltonian neural networks

1. Introduction

Synchronization refers to the process by which interacting dynamical systems adjust aspects of their motion—such as amplitude, phase, or frequency—through coupling. In neural systems, this adjustment reflects coordinated electrical activity among neurons or brain regions and plays a key role in both physiological and pathological function. Coherent synchronization supports essential cognitive processes, including perception, memory, and attention [1], whereas excessive or uncontrolled synchronization can underlie epileptic seizures and related disorders [2]. Experimental and modeling studies show that changes in synaptic strength or network connectivity can induce transitions between asynchronous, weakly synchronized, and hyper-synchronized states [3, 4]. Comprehensive reviews appear in [5, 6].

Among the various notions of synchrony—such as phase synchronization [7, 8, 9, 10, 11], cluster synchronization [12], phase-synchronized clusters [13, 14], generalized synchroniza-

Email addresses: behnam.babaeian@fau.de (Behnam Babaeian), marius.yamakou@fau.de (Marius E. Yamakou)

tion [15, 16], reduced-order synchronization [17, 18, 19, 20], and increased-order synchronization [21, 22]—we focus here on complete synchronization (CS) of same-order chaotic systems [23, 24]. In this regime, the trajectories of two coupled systems converge so that $|x_1(t) - x_2(t)| \rightarrow 0$ as $t \rightarrow \infty$ [6, 23, 25, 26]. CS provides the most direct measure of coherence and a tractable setting for Lyapunov stability analysis. Although other types—such as phase synchronization, characterized by 2π -locked phases with uncorrelated amplitudes—play essential roles in distributed brain dynamics, we emphasize CS as a foundation for understanding the energetic and structural basis of synchronization in nonlinear neurons.

Synchronization has been widely analyzed in neural models of varying complexity [27, 28, 29]. Interactions between excitatory and inhibitory populations regulate both phase and anti-phase locking [30], while coupling strength and connection probability influence the onset of spike or bursting synchronization [31]. Historically, these phenomena have been studied using classical dynamical-systems theory, providing analytical and numerical tools to characterize coherent activity. Within this framework, the present work investigates CS between two electromagnetically and memristively coupled Hindmarsh–Rose (HR) neurons. We provide a Lyapunov-based proof of asymptotic stability, corroborated by numerical simulations, and introduce a physics-informed machine-learning framework that learns the associated energy landscape directly from data.

In recent years, the physics-informed neural network (PINN) framework has become a powerful approach for solving forward and inverse problems governed by differential equations [32, 33, 34]. The key idea is to embed governing physical laws—typically expressed as ordinary or partial differential equations—directly into the learning objective. By penalizing equation residuals during training, the model enforces physical consistency and improves generalization beyond observed data [34]. For example, [33] demonstrated that causality-aware loss functions enable stable learning of chaotic and turbulent systems such as the Lorenz attractor and the Navier–Stokes equations.

A complementary development is the Hamiltonian neural network (HNN) [35], which learns the underlying energy function of a dynamical system. An HNN represents the dynamics using a learned Hamiltonian $H_\theta(x)$ together with a fixed skew-symmetric interconnection matrix enforcing energy conservation. This enables unsupervised identification of conservative dynamics from trajectory data. Extensions such as [36] and [37] incorporated structural priors, coordinate transformations, and learned symplectic forms to improve identifiability and data efficiency. Nonetheless, classical HNNs apply only to conservative systems and cannot represent dissipation or environmental interactions, which are fundamental in neuronal dynamics.

To address these limitations, HNNs were extended to port–Hamiltonian neural networks (pHNNs) [38], which generalize Hamiltonian mechanics to include energy exchange, dissipation, and external actuation. A pHNN decomposes the vector field into a skew-symmetric interconnection matrix and a symmetric positive-semidefinite dissipation matrix coupled through energy ports. The work in [39] demonstrated that such factorizations can be learned directly from data, recovering both conservative and dissipative components. More recent studies [40, 41] introduced compositional and rollout-based variants for model learning over finite prediction windows.

A parallel line of research has extended the pHNN framework to stochastic dynamical systems. The study in [42] formulated a mean-square port–Hamiltonian neural network (MS-pHNN) that decomposes stochastic dynamics into Hamiltonian drift, dissipative drift, and diffusion-induced correction terms. The authors proposed a mean-square passivity condition

for stability under noise and introduced a drift–diffusion loss enabling the learning of stochastic energy landscapes. While providing a principled formulation for stochastic pH systems, this line of work focuses on noisy mechanical oscillators and does not address synchronization or physics-informed residual training.

Despite these advances, existing pHNN methods remain computationally demanding for stiff or chaotic systems and face identifiability challenges: multiple combinations of Hamiltonian, interconnection, and dissipation terms may reproduce the same trajectories [43, 36]. This can lead to ambiguous or physically inconsistent energy representations when training is unconstrained.

Beyond general dynamical-systems modeling, these neural frameworks have growing relevance in computational neuroscience, where nonlinear oscillators such as FitzHugh–Nagumo or HR neurons display multistability, bursting, and chaotic synchronization. Physics-informed and Hamiltonian-based learning methods offer an interpretable bridge between data-driven modeling and biophysical realism. By incorporating principles such as energy conservation and dissipation, they help illuminate the energetic mechanisms underlying neuronal synchrony—a key determinant of coherent neural activity and information processing. Unifying Hamiltonian structure with physics-informed regularization thus provides a principled and biologically meaningful way to study the energetics of synchronization and decoherence in complex neural systems.

Motivated by these challenges, we retain the structural advantages of the port–Hamiltonian formulation while regularizing learning through PINN-style residual constraints. To our knowledge, no prior work has unified port–Hamiltonian factorization with physics-informed residual training in a single framework. We therefore propose the port–Hamiltonian physics-informed neural network (pH–PINN), which combines the interpretability of energy-based modeling with the consistency of residual-driven training. Specifically, the pH–PINN enforces the governing differential equations and uses a Helmholtz decomposition of the vector field to associate the divergence-free (energy-conserving) component with the Hamiltonian interconnection flow and the curl-free (dissipative) component with the non-conservative flow. This dual constraint improves identifiability, prevents degenerate energy landscapes, and alleviates the need for long rollout windows—making it well-suited for studying the energetic and stability aspects of synchronization in chaotic systems. As shown here, the pH–PINN accurately recovers both the Hamiltonian function and its time derivative, bridging analytical dynamical systems theory with data-driven discovery.

The paper is structured as follows: Section 2 introduces the 5D HR neuron model and its dynamics, illustrated through bifurcation diagrams. Section 3 establishes asymptotic stability of the synchronization manifold via Lyapunov analysis. Section 4 presents numerical simulations that corroborate the theoretical results. Section 5 develops the pH–PINN framework for data-driven learning of synchronization energetics. Finally, Section 6 summarizes the findings and discusses potential extensions.

2. Mathematical model and dynamics

We investigate a paradigmatic neuron model of established biological relevance—the HR model [44, 45]—extended to incorporate additional biophysical mechanisms. Specifically, we consider the effects of electromagnetic induction [46, 47] and an autaptic feedback current governed by a switchable memristive synapse, resulting into a new five-dimensional formulation

of the HR neuron model is given by [48]:

$$\begin{cases} \dot{x} = y - ax^3 + bx^2 + k(h + fu^2)x + \rho\phi x + I, \\ \dot{y} = c - dx^2 - y, \\ \dot{z} = r [s(x + x_0) - z], \\ \dot{u} = -u + m (|u + 1| - |u - 1|) + x, \\ \dot{\phi} = x - q\phi. \end{cases} \quad (1)$$

where x and y represent the membrane potential and the fast recovery variable, respectively, while z accounts for the slow adaptation current. The variable u denotes the internal state of the switchable memristor governing the autaptic feedback current, and ϕ represents the magnetic flux associated with electromagnetic induction. The parameters $a, b, c, d, r, s, k, h, f, m, q, \rho, x_0$, and I are real constants that control the intrinsic dynamics, coupling, and feedback strength of the system.

This formulation extends the classical three-dimensional HR model [44] by introducing two additional dynamical variables— u and ϕ —thereby capturing both electromagnetic and memristive effects. These extensions enable the model to reproduce a broad spectrum of dynamical behaviors, including bursting, chaotic oscillations, and self-modulated activity induced by autaptic feedback.

The nonlinear term $m(|u + 1| - |u - 1|)$ in Eq. (1) models the current–voltage characteristic of the switchable memristor. It provides a continuous, piecewise-linear approximation of the internal switching behavior, with the parameter m determining the memory strength of the autaptic feedback [48]. The state variable u , driven by both the membrane potential x and its decay term $-u$, introduces an adaptive self-coupling mechanism that enables activity-dependent modulation of neuronal excitability. Dynamically, this feedback acts as a nonlinear memory term that enriches the system’s phase-space structure and supports transitions between quiescent, periodic, and chaotic regimes.

Unless stated otherwise, parameters are fixed at their standard values [47]: $a = 1.0$, $b = 3.0$, $c = 1.0$, $d = 5.0$, $f = 0.2$, $h = 0.3$, $k = 0.87$, $m = 0.5$, $q = 0.005$, $r = 0.006$, $s = 5.2$, $x_0 = -1.56$, $\rho = 0.7$, $I = 0.8$, $g_e = 0.62$. The parameters k , ρ , and m are treated as bifurcation parameters and systematically varied within prescribed ranges to explore qualitative changes in the dynamics via local and global bifurcations. These parameters play key roles in shaping the system’s dynamics: the coefficient k mediates the modulation of the membrane potential x by the magnetic flux ϕ , while q characterizes the degree of polarization and magnetization by controlling flux saturation [49]. The parameter ρ governs the memory conductance associated with the magnetic flux of the memristor [49], and m quantifies the memory strength of the autaptic feedback [48]. Variations in these parameters lead to transitions among equilibrium states, periodic oscillations, and chaotic attractors, revealing a rich bifurcation structure underlying the model’s nonlinear behavior.

Due to the strong nonlinearities in Eq. (1), the system was analyzed via high-precision numerical integration. Simulations were carried out in Python using JAX [50] and DiffraX [51] with the adaptive Tsitouras 5/4 Runge–Kutta method (Tsit5) [52]. Computations employed 64-bit precision with tolerances of 10^{-8} (relative) and 10^{-10} (absolute). Each trajectory was integrated for 1000 time units from $\mathbf{x}_0 = (0, 0, 0, 1, 0)^\top$, discarding the first 500 units to remove transients. Bifurcation diagrams and Lyapunov spectra were obtained from the post-transient local maxima of $x(t)$, and Lyapunov exponents were computed using the Benettin

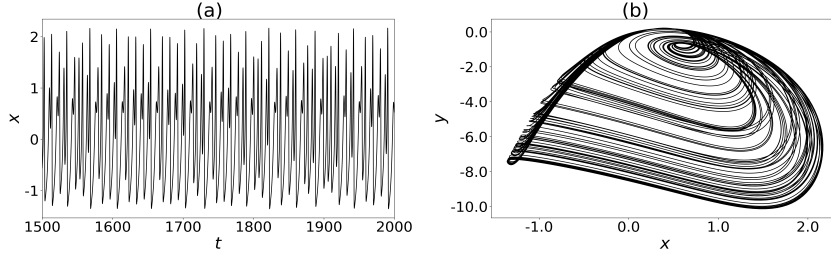


Figure 1: Chaotic time series of the x variable **(a)** and corresponding phase portrait in the $x - y$ plane **(b)** with $k = 0.87$, $m = 0.5$ and $\rho = 0.7$.

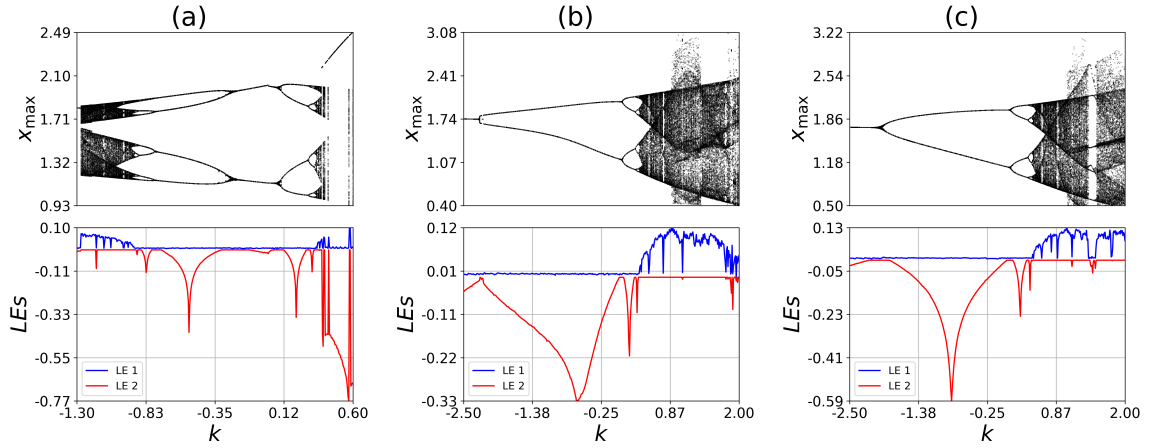


Figure 2: Bifurcation diagrams and the two largest Lyapunov exponents versus k at $\rho = 0.7$ for different values of m : **(a)** $m = 1$, **(b)** $m = 0.5$, **(c)** $m = 0.25$.

algorithm with periodic orthonormalization. The resulting bifurcation structures are shown in Figs. 2–4.

Figure 1 shows a chaotic time series of the x variable **(a)** and corresponding phase portrait in the $x - y$ plane **(b)** for the 5D HR neuron model in Eq. (1). The model exhibits a rich spectrum of dynamical behaviors.

Figure 2 shows the bifurcation diagrams and the two largest Lyapunov exponents versus k for fixed $\rho = 0.7$ and different m . As k increases, the system exhibits a period-doubling route to chaos, while smaller m values suppress chaotic oscillations.

Figure 3 presents the corresponding diagrams versus ρ at fixed $k = 0.87$. Increasing ρ induces transitions between periodic and chaotic regimes, with the range of chaos shrinking as m decreases.

Figure 4 displays two-dimensional maps of the largest Lyapunov exponent in the (k, m) , (ρ, m) , and (ρ, k) planes. Reddish–yellow regions mark chaotic dynamics, delineating the global organization of periodic and chaotic attractors in parameter space.

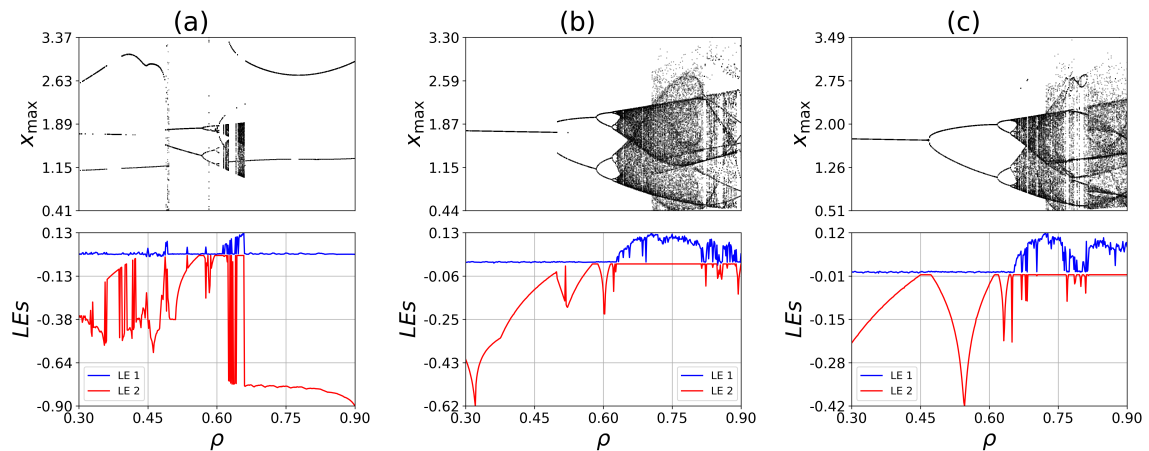


Figure 3: Bifurcation diagrams and the two largest Lyapunov exponents versus ρ at $k = 0.87$ for different values of m : (a) $m = 1$, (b) $m = 0.5$, (c) $m = 0.25$.

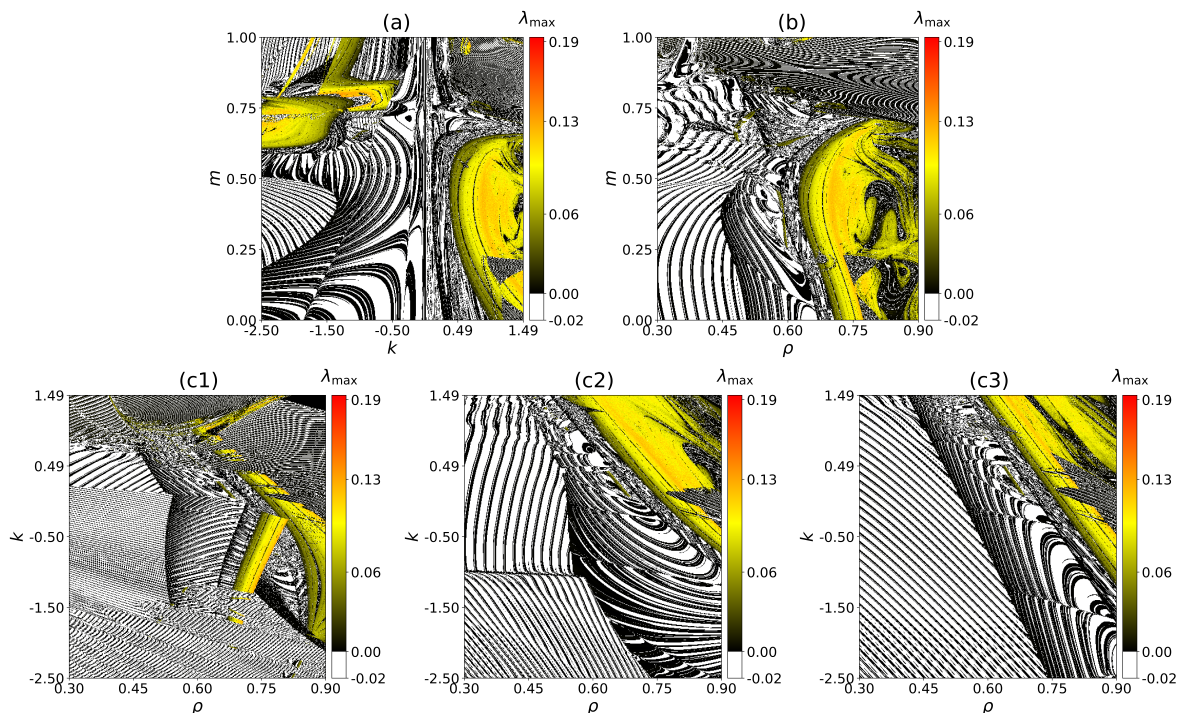


Figure 4: Two-dimensional dynamical maps for different parameter pairs: (a) (k, m) at fixed $\rho = 0.7$; (b) (ρ, m) at fixed $k = 0.87$; (c1–c3) (ρ, k) at fixed $m = 1, 0.5$, and 0.25 , respectively.

3. Stable chaotic synchronization energy: A dynamical systems approach

In this section, we investigate the stability of CS between two diffusively coupled chaotic 5D HR neurons governed by Eq. (1), together with the associated synchronization energy. The analysis is conducted within the framework of dynamical systems theory, employing Lyapunov stability analysis [53] to evaluate the onset and robustness of synchronization, and Helmholtz's theorem [54] to characterize the energetic aspects of the synchronized state.

Particular attention is devoted to the asymptotic stability of the synchronization manifold and to the behavior of the synchronization energy under variations of the key system parameters.

3.1. Asymptotic stability proof of the synchronization manifold

We consider two identical HR neurons coupled diffusively through their membrane potentials. The coupled system is written as

$$\begin{cases} \dot{x}_i = y_i - ax_i^3 + bx_i^2 + k(h + fu_i^2)x_i + \rho\phi_i x_i + I_i + g_e \sum_{j=1}^2 \xi_{ij}(x_j - x_i), \\ \dot{y}_i = c - dx_i^2 - y_i, \\ \dot{z}_i = r [s(x_i + x_0) - z_i], \\ \dot{u}_i = -u_i + m (|u_i + 1| - |u_i - 1|) + x_i, \\ \dot{\phi}_i = x_i - q\phi_i, \end{cases} \quad (2)$$

where g_e denotes the electrical (gap-junction) coupling strength that determines the intensity of interaction between neurons. The coupling topology is defined by $\xi_{ij} = 1$ for $i \neq j$, indicating mutual coupling between neurons i and j , and $\xi_{ij} = 0$ otherwise. For the two-neuron system considered here, $\xi_{12} = \xi_{21} = 1$. This formulation provides the mathematical basis for studying how the interplay between intrinsic neuronal dynamics and diffusive coupling gives rise to collective synchronization.

Definition 3.1. Two chaotic systems $x(t), y(t) \in \mathbb{R}^n$ are said to achieve CS if there exist initial conditions $x(t_0) = x_0$ and $y(t_0) = y_0$ such that

$$\lim_{t \rightarrow \infty} \|x(t) - y(t)\| = 0. \quad (3)$$

The synchronized state is represented by the invariant manifold

$$\mathcal{M} = \{\mathbf{x}_1 = \mathbf{x}_2 = \mathbf{x}_s\}, \quad (4)$$

where $\mathbf{x}_s = (x_s, y_s, z_s, u_s, \phi_s)^\top$ evolves according to the uncoupled dynamics given in Eq. (1). To investigate the global asymptotic stability of \mathcal{M} , we introduce the synchronization error system via

$$\begin{cases} \dot{e}_x = \dot{x}_2 - \dot{x}_1, \\ \dot{e}_y = \dot{y}_2 - \dot{y}_1, \\ \dot{e}_z = \dot{z}_2 - \dot{z}_1, \\ \dot{e}_u = \dot{u}_2 - \dot{u}_1, \\ \dot{e}_\phi = \dot{\phi}_2 - \dot{\phi}_1. \end{cases} \quad (5)$$

By taking the difference between the equations of the two coupled neurons, one arrives at the corresponding error dynamics. Discarding higher-order nonlinear contributions in the error variables $(e_x^2, e_x^3, e_u^2, e_x e_\phi)$, we obtain the linearized error system that describes the most

significant transverse deviations from \mathcal{M} :

$$\left\{ \begin{array}{l} \dot{e}_x = \left[-3ax_1^2 + 2bx_1 + k(h + fu_1^2) + \rho\phi_1 - 2g_e \right] e_x + e_y + 2kfx_1u_1e_u + \rho x_1e_\phi, \\ \dot{e}_y = -2dx_1e_x - e_y, \\ \dot{e}_z = r(se_x - e_z), \\ \dot{e}_u = \begin{cases} e_x + (2m-1)e_u + 2m(u_1-1), & \text{if } u_1 \geq 1, -1 < u_2 < 1, \\ e_x - e_u - 4m, & \text{if } u_1 \geq 1, u_2 \leq -1, \\ e_x - e_u - 2m(u_1-1), & \text{if } -1 < u_1 < 1, u_2 \geq 1, \\ e_x + (2m-1)e_u, & \text{if } -1 < u_1 < 1, -1 < u_2 < 1, \\ e_x - e_u - 2m(u_1+1), & \text{if } -1 < u_1 < 1, u_2 \leq -1, \\ e_x - e_u + 4m, & \text{if } u_1 \leq -1, u_2 \geq 1, \\ e_x + (2m-1)e_u + 2m(u_1+1), & \text{if } u_1 \leq -1, -1 < u_2 < 1, \\ e_x - e_u, & \text{otherwise,} \end{cases} \\ \dot{e}_\phi = e_x - qe_\phi. \end{array} \right. \quad (6)$$

Theorem 3.2. *The coupled chaotic systems in Eq. (2) achieve CS if the five ordered principal minors in Eq. (15) are all sufficiently positive.*

Proof. We define the quadratic Lyapunov candidate $V : \mathbb{R}^5 \rightarrow \mathbb{R}_{\geq 0}$ by

$$V(e_x, e_y, e_z, e_u, e_\phi) = \frac{1}{2} (e_x^2 + e_y^2 + e_z^2 + e_u^2 + e_\phi^2). \quad (7)$$

Along trajectories of the error dynamics Eq. (6),

$$\dot{V} = e_x \dot{e}_x + e_y \dot{e}_y + e_z \dot{e}_z + e_u \dot{e}_u + e_\phi \dot{e}_\phi. \quad (8)$$

Since the neurons evolve on bounded chaotic attractors, we can assert the existence of a constant $J > 0$ such that

$$|x_1(t)| \leq J, \quad |u_1(t)| \leq J, \quad |\phi_1(t)| \leq J, \quad \forall t \geq 0. \quad (9)$$

Inserting Eq. (6) into the expression for \dot{V} and applying these bounds termwise, we obtain the upper estimate

$$\begin{aligned} \dot{V} \leq & \left[3|a|J^2 + 2|b|J + |kh| + |kf|J^2 + |\rho|J - 2|g_e| \right] e_x^2 - e_y^2 - |r|e_z^2 - |q|e_\phi^2 \\ & + (1 + 2|d|J)|e_x||e_y| + |rs||e_x||e_z| + (2|kf|J^2 + 1)|e_x||e_u| + (|\rho|J + 1)|e_x||e_\phi| \\ & + \Psi(e_u; u_1, u_2, m, J), \end{aligned} \quad (10)$$

where $\Psi(e_u; u_1, u_2, m, J)$ collects the contribution coming from the memristive term and is explicitly given by

$$\Psi(e_u; u_1, u_2, m, J) = \begin{cases} |2m-1|e_u^2 + 2|m|(J-1)|e_u|, & \text{if } u_1 \geq 1, -1 < u_2 < 1, \\ -e_u^2 - 4|m|e_u, & \text{if } u_1 \geq 1, u_2 \leq -1, \\ -e_u^2 - 2|m|(J-1)e_u, & \text{if } -1 < u_1 < 1, u_2 \geq 1, \\ |2m-1|e_u^2, & \text{if } -1 < u_1 < 1, -1 < u_2 < 1, \\ -e_u^2 - 2|m|(J+1)e_u, & \text{if } -1 < u_1 < 1, u_2 \leq -1, \\ -e_u^2 + 4|m|e_u, & \text{if } u_1 \leq -1, u_2 \geq 1, \\ |2m-1|e_u^2 + 2|m|(J+1)e_u, & \text{if } u_1 \leq -1, -1 < u_2 < 1, \\ -e_u^2, & \text{otherwise.} \end{cases} \quad (11)$$

The bound in Eq. (10) can be recast in matrix notation as

$$\dot{V} \leq -\mathbf{E}^\top \mathbf{M} \mathbf{E} - |e_u| \Psi(e_u; u_1, u_2, m, J), \quad (12)$$

where $\mathbf{E}^\top = (|e_x|, |e_y|, |e_z|, |e_u|, |e_\phi|)$ denotes the vector of absolute error components and \mathbf{M} is the symmetric matrix

$$\mathbf{M} = \begin{bmatrix} A_{xx} & A_{xy} & A_{xz} & A_{xu} & A_{x\phi} \\ A_{yx} & 1 & 0 & 0 & 0 \\ A_{zx} & 0 & |r| & 0 & 0 \\ A_{ux} & 0 & 0 & A_{uu} & 0 \\ A_{\phi x} & 0 & 0 & 0 & |q| \end{bmatrix}, \quad (13)$$

with entries specified by

$$\left\{ \begin{array}{l} A_{xy} = A_{yx} = -\frac{1}{2}(1 + 2|d|J), \\ A_{xz} = A_{zx} = -\frac{1}{2}|rs|, \\ A_{xu} = A_{ux} = -\frac{1}{2}(2|kf|J^2 + 1), \\ A_{x\phi} = A_{\phi x} = -\frac{1}{2}(|\rho|J + 1), \\ A_{xx} = -3|a|J^2 - 2|b|J - |kh| - |kf|J^2 - |\rho|J + 2|g_e|, \\ A_{uu} = \begin{cases} -|2m - 1| & \text{if } u_1 \geq 1 \text{ and } -1 < u_2 < 1, \\ 1 & \text{if } u_1 \geq 1 \text{ and } u_2 \leq -1, \\ 1 & \text{if } -1 < u_1 < 1 \text{ and } u_2 \geq 1, \\ -|2m - 1| & \text{if } -1 < u_1 < 1 \text{ and } -1 < u_2 < 1, \\ 1 & \text{if } -1 < u_1 < 1 \text{ and } u_2 \leq -1, \\ 1 & \text{if } u_1 \leq -1 \text{ and } u_2 \geq 1 \\ -|2m - 1| & \text{if } u_1 \leq -1 \text{ and } -1 < u_2 < 1, \\ 1 & \text{elsewhere.} \end{cases} \end{array} \right. \quad (14)$$

The fixed point $e_i^* = 0$, $i = x, y, z, u, \phi$ of the error system Eq. (6) will be Lyapunov stable once the right-hand side of Eq. (12) is nonpositive. This is guaranteed whenever the quadratic form $-\mathbf{E}^\top \mathbf{M} \mathbf{E}$ compensates all potentially positive contributions coming from the memristive term $\Psi(e_u; u_1, u_2, m, J)$, which is ensured by sufficiently strong positive definiteness of \mathbf{M} .

Lemma 3.3 (Sylvester's Criterion). *Let A be a real symmetric matrix. Then A is positive definite if and only if each of its leading principal minors is strictly positive.*

Evaluating the leading principal minors of \mathbf{M} yields

$$\begin{cases}
D_1 = -3|a|J^2 - 2|b|J - |kh| - |kf|J^2 - |\rho|J + 2|g_e|, \\
D_2 = D_1 - \frac{1}{4}(1 + 2|d|J)^2, \\
D_3 = |r|D_2 - \frac{1}{4}|rs|^2, \\
D_4 = \begin{cases} -|2m-1|D_3 - \frac{|r|}{4}(2|kf|J^2 + 1)^2, & \text{if } u_1 \geq 1, -1 < u_2 < 1, \\ D_3 - \frac{|r|}{4}(2|kf|J^2 + 1)^2, & \text{if } u_1 \geq 1, u_2 \leq -1, \\ D_3 - \frac{|r|}{4}(2|kf|J^2 + 1)^2, & \text{if } -1 < u_1 < 1, u_2 \geq 1, \\ -|2m-1|D_3 - \frac{|r|}{4}(2|kf|J^2 + 1)^2, & \text{if } -1 < u_1 < 1, -1 < u_2 < 1, \\ D_3 - \frac{|r|}{4}(2|kf|J^2 + 1)^2, & \text{if } -1 < u_1 < 1, u_2 \leq -1, \\ D_3 - \frac{|r|}{4}(2|kf|J^2 + 1)^2, & \text{if } u_1 \leq -1, u_2 \geq 1, \\ -|2m-1|D_3 - \frac{|r|}{4}(2|kf|J^2 + 1)^2, & \text{if } u_1 \leq -1, -1 < u_2 < 1, \\ D_3 - \frac{|r|}{4}(2|kf|J^2 + 1)^2, & \text{elsewhere.} \end{cases} \\
D_5 = \begin{cases} |q|D_4 + \frac{|r||2m-1|}{4}(|\rho|J + 1)^2, & \text{if } u_1 \geq 1, -1 < u_2 < 1, \\ |q|D_4 - \frac{|r|}{4}(|\rho|J + 1)^2, & \text{if } u_1 \geq 1, u_2 \leq -1, \\ |q|D_4 - \frac{|r|}{4}(|\rho|J + 1)^2, & \text{if } -1 < u_1 < 1, u_2 \geq 1, \\ |q|D_4 + \frac{|r||2m-1|}{4}(|\rho|J + 1)^2, & \text{if } -1 < u_1 < 1, -1 < u_2 < 1, \\ |q|D_4 - \frac{|r|}{4}(|\rho|J + 1)^2, & \text{if } -1 < u_1 < 1, u_2 \leq -1, \\ |q|D_4 - \frac{|r|}{4}(|\rho|J + 1)^2, & \text{if } u_1 \leq -1, u_2 \geq 1, \\ |q|D_4 + \frac{|r||2m-1|}{4}(|\rho|J + 1)^2, & \text{if } u_1 \leq -1, -1 < u_2 < 1, \\ |q|D_4 - \frac{|r|}{4}(|\rho|J + 1)^2, & \text{elsewhere.} \end{cases}
\end{cases} \quad (15)$$

Choosing the parameters $\{a, b, d, f, h, k, m, q, r, s, \rho, g_e\}$ such that all minors in Eq. (15) are strictly positive ensures $\mathbf{M} \succ 0$, and hence $\dot{V} \leq 0$. In this situation, V is positive definite and decrescent, so the fixed point $e_i^* = 0$, $i = x, y, z, u, \phi$, of the error system Eq. (6) is Lyapunov stable.

To strengthen this to global asymptotic stability of $e_i^* = 0$, we must additionally show that errors decay to zero, i.e., that transverse perturbations to the synchronization manifold \mathcal{M} vanish as $t \rightarrow \infty$. From Eqs. (7) and (12), the error components are uniformly bounded, $e_i \in L^\infty$ for $i = x, y, z, u, \phi$. Consequently, the right-hand side of Eq. (6) is also bounded, and thus $\dot{e}_i \in L^\infty$ for each component.

Next, decompose (12) as $\dot{V} \leq \dot{V}_1 + \dot{V}_2$, where $\dot{V}_1 = -\mathbf{e}^\top \mathbf{M} \mathbf{e}$ and $\dot{V}_2 = -|e_u| \Psi(e_u; u_1, u_2, m, J)$. Integrating the contribution from \dot{V}_1 yields

$$\begin{aligned}
\int_0^t \mathbf{e}(s)^\top \mathbf{M} \mathbf{e}(s) ds &= - \int_0^t \dot{V}_1(s) ds \\
&= V_1(0) - V_1(t) \leq V_1(0).
\end{aligned} \quad (16)$$

Lemma 3.4. (*Rayleigh bound*). For any nonzero vector $x \in \mathbb{R}^n$ and any symmetric matrix $A \in \mathbb{R}^{n \times n}$, the quadratic form satisfies $x^\top A x \geq \lambda_{\min}(A) \|x\|^2$, where $\lambda_{\min}(A)$ denotes the smallest eigenvalue of A .

Combining Eq. (16) with Lemma 3.4, we obtain the estimate

$$\int_0^t \|\mathbf{e}(s)\| ds \leq V_1(0)/\lambda_{\min}(\mathbf{M}), \quad (17)$$

where $\lambda_{\min}(\mathbf{M})$ is the minimum eigenvalue of the positive definite matrix \mathbf{M} .

Lemma 3.5. (*Barbalat's Lemma*). Let $f : [0, \infty) \rightarrow \mathbb{R}$ be a uniformly continuous function such that $\lim_{t \rightarrow \infty} \int_0^t f(s) ds < \infty$. Then $\lim_{t \rightarrow \infty} f(t) = 0$.

From Eqs. (16)–(17) and Lemma 3.5, it follows that, for any initial condition,

$$\lim_{t \rightarrow \infty} \|e_i(t)\| = 0, \quad i = x, y, z, u, \phi. \quad (18)$$

Therefore, the coupled chaotic systems in Eq. (2) synchronize globally and asymptotically in the sense of CS. \square

Numerical simulations are provided in Sect. 4 to corroborate the effectiveness of the Theorem 3.2.

3.2. Synchronization energy

According to Helmholtz's theorem [54], any smooth vector field $\mathbf{F}(\mathbf{r})$ of a dynamical system can be decomposed into a conservative (divergence-free) part $\mathbf{F}_c(\mathbf{r})$ and a dissipative (curl-free) part $\mathbf{F}_d(\mathbf{r})$:

$$\mathbf{F}(\mathbf{r}) = \mathbf{F}_c(\mathbf{r}) + \mathbf{F}_d(\mathbf{r}), \quad (19)$$

where the conservative component governs rotational motion, while the dissipative component governs energy exchange with the environment. The divergence-free (conservative) and curl-free (dissipative) vector fields of the error dynamical system in Eq. (6) are respectively given by

$$\mathbf{F}_c(\mathbf{e}) = \begin{pmatrix} e_y + 2kf u_1 x_1 e_u + \rho x_1 e_\phi \\ -2d x_1 e_x \\ r s e_x \\ e_x \\ e_x \end{pmatrix}, \quad \mathbf{F}_d(\mathbf{e}) = \begin{pmatrix} N(x_1, u_1, \phi_1) e_x \\ -e_y \\ -r e_z \\ \alpha(u_1, u_2) e_u + \beta(u_1, u_2) \\ -q e_\phi \end{pmatrix}, \quad (20)$$

where

$$\left\{ \begin{array}{l} N(x_1, u_1, \phi_1) = -3a x_1^2 + 2b x_1 + kh + kf u_1^2 + \rho \phi_1 - 2g_e, \\ \alpha(u_1, u_2) = \begin{cases} 2m - 1, & \text{if } u_1 \geq 1, -1 < u_2 < 1, \\ -1, & \text{if } u_1 \geq 1, u_2 \leq -1, \\ -1, & \text{if } -1 < u_1 < 1, u_2 \geq 1, \\ 2m - 1, & \text{if } -1 < u_1 < 1, -1 < u_2 < 1, \\ -1, & \text{if } -1 < u_1 < 1, u_2 \leq -1, \\ -1, & \text{if } u_1 \leq -1, u_2 \geq 1, \\ 2m - 1, & \text{if } u_1 \leq -1, -1 < u_2 < 1, \\ -1, & \text{otherwise,} \end{cases} \\ \beta(u_1, u_2) = \begin{cases} 2m(u_1 - 1), & \text{if } u_1 \geq 1, -1 < u_2 < 1, \\ -4m, & \text{if } u_1 \geq 1, u_2 \leq -1, \\ -2m(u_1 - 1), & \text{if } -1 < u_1 < 1, u_2 \geq 1, \\ 0, & \text{if } -1 < u_1 < 1, -1 < u_2 < 1, \\ -2m(u_1 + 1), & \text{if } -1 < u_1 < 1, u_2 \leq -1, \\ 4m, & \text{if } u_1 \leq -1, u_2 \geq 1, \\ 2m(u_1 + 1), & \text{if } u_1 \leq -1, -1 < u_2 < 1, \\ 0, & \text{otherwise.} \end{cases} \end{array} \right. \quad (21)$$

For the conservative vector field, Eq. (20) yields a first-order linear partial differential equation (PDE) for the Hamilton energy function:

$$\left(e_y + 2kf u_1 x_1 e_u + \rho x_1 e_\phi \right) \frac{\partial H}{\partial e_x} - 2d x_1 e_x \frac{\partial H}{\partial e_y} + rs e_x \frac{\partial H}{\partial e_z} + e_x \frac{\partial H}{\partial e_u} + e_x \frac{\partial H}{\partial e_\phi} = 0, \quad (22)$$

which, by the method of separation of variables, admits the solution

$$H(e_x, e_y, e_z, e_u, e_\phi) = 2d x_1 e_x^2 + e_y^2 - 4dkf u_1 x_1^2 e_u^2 - 2d\rho x_1^2 e_\phi^2 + e_z - rs e_\phi + C, \quad (23)$$

where C is an arbitrary integration constant.

For the dissipative vector field, Eq. (20) gives the differential equation governing the time evolution of the Hamilton energy:

$$\begin{aligned} \frac{dH}{dt} = & 4d x_1 N(x_1, u_1, \phi_1) e_x^2 - 2e_y^2 - r e_z - 8dkf u_1 x_1^2 \alpha(u_1, u_2) e_u^2 \\ & - 8dkf u_1 x_1^2 \beta(u_1, u_2) e_u + 4d\rho q x_1^2 e_\phi^2 + qrs e_\phi. \end{aligned} \quad (24)$$

The synchronization energy function $H(e_x, e_y, e_z, e_u, e_\phi)$ in Eq. (23) represents the instantaneous energy stored in the synchronization manifold, while its temporal derivative dH/dt quantifies the energy flow associated with the synchronization process. A positive dH/dt indicates net energy absorption (external energy input required to sustain synchrony), whereas a negative value corresponds to energy dissipation through coupling and intrinsic neuronal losses.

This formulation provides a quantitative measure of the energetic cost of synchronization: it defines the amount of energy per unit time required to maintain a given degree of synchrony. Consequently, variations in H and dH/dt under changes of system parameters reveal how coupling strength, dissipation, and intrinsic neuronal dynamics jointly determine both the stability and the energetic efficiency of the synchronized state [47]. The numerical simulations of H and dH/dt are provided in Sect. 4.

4. Numerical simulations and discussion

To corroborate the analytical results of Theorem 3.2 and the energy-based analysis of Section 3.2, we performed numerical simulations of the coupled memristive HR neuron system in Eq. (2) and its corresponding synchronization-error dynamics in Eq. (6). The two neurons were initialized with slightly different values in all five state variables to induce synchronization transients. We then computed the time evolution of the error variables $(e_x, e_y, e_z, e_u, e_\phi)$, together with the Lyapunov and Hamilton energy derivatives \dot{V} and \dot{H} , and analyzed their dependence on the parameters m, k, ρ , and g_e .

Figure 5 shows the temporal evolution of the five synchronization-error components, each representing the difference between corresponding variables of the two coupled neurons. All error trajectories decay asymptotically to zero after a brief transient, confirming CS. The fast variables e_x, e_y, e_u, e_ϕ converge earlier than the slow adaptation variable e_z , reflecting the intrinsic separation of time scales in the neuron dynamics. These results corroborate the theoretical prediction that the synchronization manifold $\mathcal{M} = \{x_1 = x_2, \dots, \phi_1 = \phi_2\}$ is globally asymptotically stable under the given parameter values and coupling conditions.

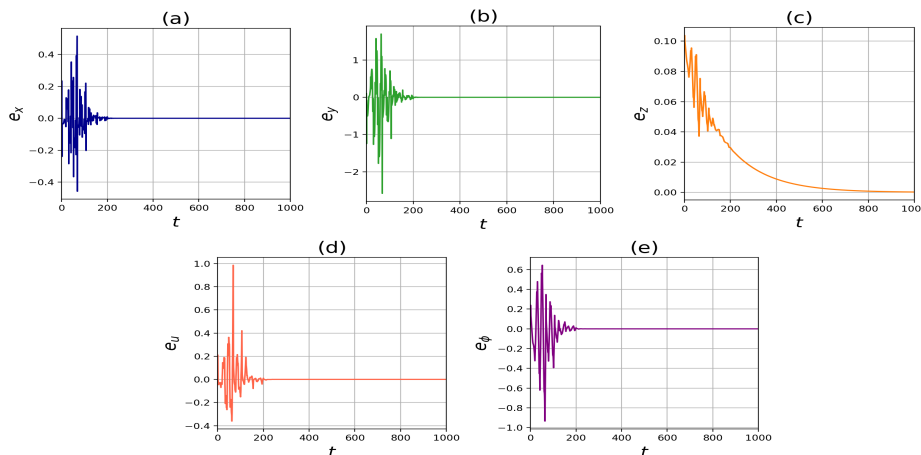


Figure 5: (a)-(e): Time evolution of the five synchronization-error components $(e_x, e_y, e_z, e_u, e_\phi)$, respectively, showing convergence to zero.

Figure 6 presents the temporal evolution of the synchronization Hamiltonian $H(e_x, e_y, e_z, e_u, e_\phi)$ and its derivative \dot{H} associated to the errors in Fig. 5. The Hamiltonian decays monotonically to zero as the neurons approach synchrony. The derivative \dot{H} exhibits transient oscillations, taking both negative and positive values before stabilizing near zero; this reflects intermittent energy exchange due to memristive and flux-related terms in the dynamics. After transients, $\dot{H} \rightarrow 0$ and the system settles on the synchronization manifold, consistent with an overall dissipative relaxation toward synchrony.

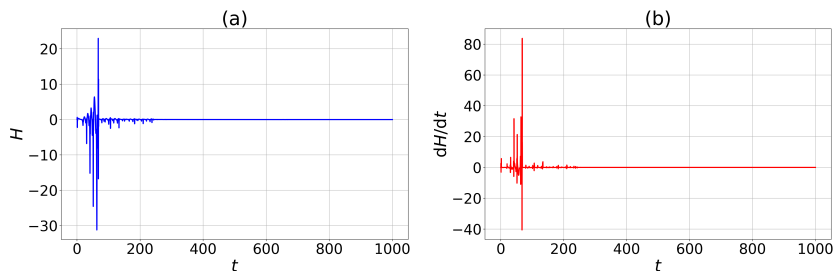


Figure 6: Time evolution of the error-system Hamiltonian function **(a)** and its time derivative **(b)**, corresponding to the errors shown in Figure 5; as the system synchronizes, both energy and its derivative approach zero.

Figure 7 compares the time-averaged derivatives of the Lyapunov function \dot{V} and the Hamiltonian function \dot{H} as functions of the main control parameters m , k , ρ , and g_e . Each data point corresponds to a post-transient average over a long trajectory. Both measures exhibit nearly identical qualitative and quantitative results across all parameters, confirming the consistency between the Lyapunov and Hamiltonian formulations. Increasing g_e or reducing m enhances dissipation and accelerates synchronization, whereas larger ρ or k increase the energy input required for synchrony.

These findings further highlight the deep correspondence between Lyapunov-based and Hamiltonian-based characterizations of stability and energetic regulation in chaotic synchronization. In particular, the fact that \dot{V} and \dot{H} exhibit the same qualitative behavior implies that the Hamiltonian can serve as an effective stability certificate. This is especially valuable in situations where a suitable Lyapunov function V is difficult to construct or analytically intractable, whereas the Hamiltonian structure is readily available or naturally derived from the port-Hamiltonian formulation. Thus, the Hamiltonian offers a principled and computationally accessible alternative for assessing convergence toward the synchronization manifold.

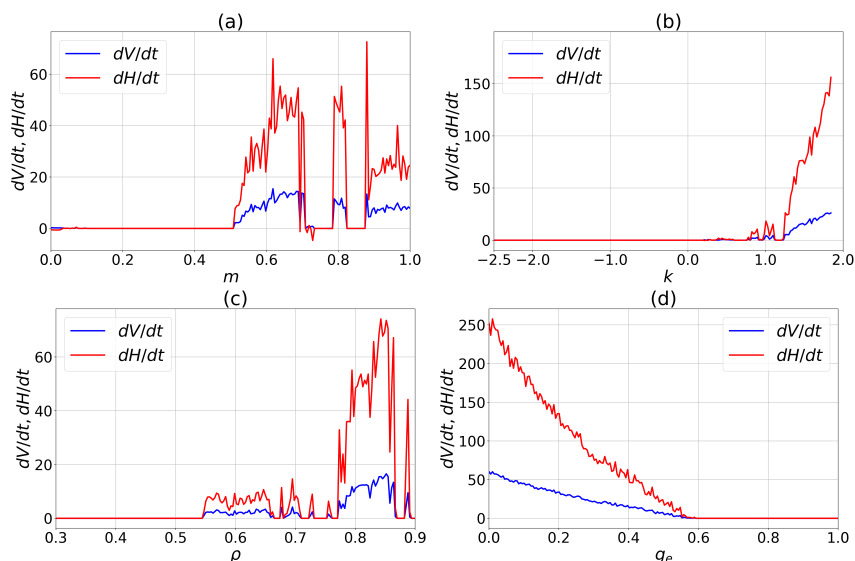


Figure 7: Time derivatives of the Lyapunov and Hamiltonian functions plotted as functions of the parameters m and k in panels (a)–(b), and ρ and g_e in panels (c)–(d). In all cases, \dot{V} and \dot{H} exhibit the same qualitative trends, confirming the consistency between the Lyapunov and Hamiltonian stability assessments.

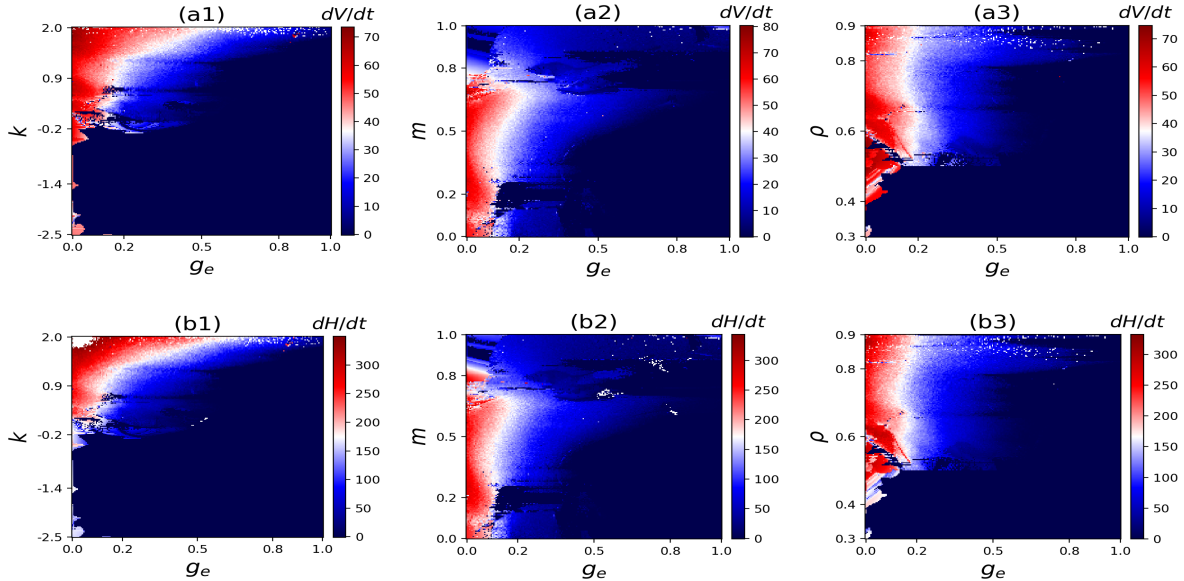


Figure 8: Heatmaps of the time derivatives of the Lyapunov function (a1)–(a3) and the corresponding Hamiltonian function (b1)–(b3) as functions of g_e and the system parameters k , m , and ρ , respectively. Across all parameter pairs, \dot{V} and \dot{H} display consistent qualitative trends, demonstrating a robust correspondence between Lyapunov-based and Hamiltonian-based stability indicators.

Figure 8 presents heatmaps of \dot{V} (first row) and the corresponding \dot{H} (second row) as functions of the coupling strength g_e and the intrinsic parameters k , m , and ρ . The color gradients represent the mean post-transient energy-dissipation rate. In all panels, dark blue regions correspond to parameter combinations yielding rapid and stable synchronization. The close agreement between the \dot{V} and \dot{H} maps confirms that both measures capture the same dissipative structure of the system. Efficient synchronization occurs for intermediate m and sufficiently large g_e , whereas strong flux coupling (k, ρ large) can destabilize the manifold by injecting excess energy. These results emphasize how electrical, magnetic, and memristive couplings jointly determine both the rate and energetic cost of neuronal synchrony.

In summary, the numerical results confirm the analytical predictions of Section 3. The coupled neurons exhibit global asymptotic CS, with the Hamiltonian energy decaying monotonically to zero and the Lyapunov and Hamiltonian formulations yielding consistent measures of stability and energetics. These findings provide a basis for the pH-PINN framework introduced in Section 5, which exploits the equivalence between Lyapunov and Hamiltonian descriptions to learn the underlying energy structure directly from data, bridging analytical theory with machine-learning discovery of energy-conserving and dissipative dynamics.

5. A port-Hamiltonian physics-informed neural network (pH-PINN) approach

To study synchronization energy of the coupled HR neurons in Eq. (2) from a data-driven perspective, we employ a pH-PINN. This framework is well-suited to our system, whose synchronization behavior admits a Hamiltonian energy structure consistent with the pH formulation of conservative and dissipative flows. Analytical Hamiltonian approaches can establish stability but often become infeasible for high-dimensional or partially known systems. In such settings, the governing physical laws, such as energy conservation and

dissipation, remain valid even when the explicit equations are unknown. The pH-PINN incorporates these physical constraints into the learning process, allowing the synchronization energy and its dynamics to be inferred directly from data. Here, the known analytical energy serves as a benchmark to quantitatively validate the learned representation. In the sequel, we briefly outline the principles of PINNs, HNNs, and pHNNs, and describe how these are integrated to construct the proposed pH-PINN framework.

5.1. Physics-informed neural networks (PINNs)

PINN [32] embeds the governing differential equations directly into the training objective. For a system

$$\dot{\mathbf{x}} = \mathbf{f}(\mathbf{x}), \quad \mathbf{x} \in \mathbb{R}^n, \quad \mathbf{f} : \mathbb{R}^n \rightarrow \mathbb{R}^n, \quad (25)$$

let $\dot{\mathbf{x}}_\theta(\mathbf{x}) \equiv \mathbf{f}_\theta(\mathbf{x})$ denote a neural approximation of the vector field. Given data or collocation samples $\{(\mathbf{x}_i, \dot{\mathbf{x}}_i)\}_{i=1}^B$, a PINN minimizes the residual of the governing equation:

$$\mathcal{L}_{\text{PDE}} = \frac{1}{B} \sum_{i=1}^B \left\| \dot{\mathbf{x}}_i - \mathbf{f}_\theta(\mathbf{x}_i) \right\|^2, \quad (26)$$

where the equations act as soft physical constraints that bias learning toward dynamically consistent solutions and improve generalization beyond purely data-driven fitting. This residual formulation also includes structure-generated vector fields derived from learned scalar potentials, leading naturally to HNNs.

5.2. Hamiltonian neural networks (HNNs)

HNNs [35] employ a scalar-valued network $H_\theta : \mathbb{R}^n \rightarrow \mathbb{R}$ that maps the state vector \mathbf{x} to an energy $H_\theta(\mathbf{x})$. Automatic differentiation provides the gradient $\nabla H_\theta(\mathbf{x})$, representing partial derivatives of H_θ with respect to the state components. Rather than predicting the vector field directly, the dynamics are recovered through a (possibly state-dependent) skew-symmetric matrix $\mathbf{J}(\mathbf{x}) \in \mathbb{R}^{n \times n}$:

$$\dot{\mathbf{x}}_\theta(\mathbf{x}) = \mathbf{J}(\mathbf{x}) \nabla H_\theta(\mathbf{x}). \quad (27)$$

Training minimizes the mismatch between the induced field $\dot{\mathbf{x}}_\theta$ and reference derivatives $\dot{\mathbf{x}}$ (from data or automatic differentiation) as in the PINN framework. Classical HNNs use the canonical symplectic matrix \mathbf{J}_c , yielding the standard Hamiltonian form $\dot{\mathbf{x}} = (\partial H / \partial \mathbf{p}, -\partial H / \partial \mathbf{q})^\top$. For complex or noncanonical systems, however, $\mathbf{J}(\mathbf{x})$ may be learned as a separate neural network to capture generalized symplectic structures [37].

5.3. Port-Hamiltonian neural networks (pHNN)

Hamiltonian neural networks can be extended to the pH setting by augmenting the conservative Hamiltonian flow with an additional symmetric matrix \mathbf{R} . While HNNs describe ideally conservative systems, many dynamical systems exhibit extra non-conservative effects, which the pH formalism represents together with the conservative part [38]. See also [39] for a neural implementation.

$$\dot{\mathbf{x}} = \left[\mathbf{J}(\mathbf{x}) - \mathbf{R}(\mathbf{x}) \right] \nabla H_\theta(\mathbf{x}). \quad (28)$$

Here, \mathbf{J} encodes power-conserving interconnections, and $\mathbf{R} \in \mathbb{R}^{n \times n}$ represents a non-conservative part of the dynamics. The energy rate satisfies

$$\dot{H}_\theta = \nabla H_\theta^\top (\mathbf{J} - \mathbf{R}) \nabla H_\theta = -\nabla H_\theta^\top \mathbf{R} \nabla H_\theta, \quad (29)$$

since $\nabla H_\theta^\top \mathbf{J} \nabla H_\theta = 0$ for any skew-symmetric \mathbf{J} . Thus, the pH formulation makes the energetic structure explicit: the conservative flow preserves H_θ and the non-conservative part determines its time evolution.

5.4. Port–Hamiltonian physics-informed neural network (pH-PINN)

We extend the conventional pHNN (Eq. (28)) to a physics-informed framework by embedding the Helmholtz decomposition of the error dynamics as explicit training constraints. Specifically, we incorporate the analytical conservative and non-conservative fields of the linearized error system in Eq. (20) (derived from Eq. (6)) into the pH factorization following the generalized Hamiltonian approach [55, 56].

Let H_θ , $\mathbf{J}_\phi(\mathbf{e})$, and $\mathbf{R}_\psi(\mathbf{e})$ define the pHNN. The resulting pH-PINN minimizes the composite loss

$$\mathcal{L}_{\text{Total}} = \lambda_{\text{DynRes}} \mathcal{L}_{\text{DynRes}} + \lambda_J \mathcal{L}_J + \lambda_R \mathcal{L}_R + \lambda_{\text{Cons}} \mathcal{L}_{\text{Cons}} + \lambda_{\dot{H}} \mathcal{L}_{\dot{H}}, \quad (30)$$

where, over a batch $\{(\mathbf{e}_i, \dot{\mathbf{e}}_i^{\text{true}})\}_{i=1}^B$,

$$\left\{ \begin{array}{l} \mathcal{L}_{\text{DynRes}} = \frac{1}{B} \sum_{i=1}^B \left\| \dot{\mathbf{e}}_i^{\text{true}} - [\mathbf{J}_\phi(\mathbf{e}_i) - \mathbf{R}_\psi(\mathbf{e}_i)] \nabla H_\theta(\mathbf{e}_i) \right\|^2, \\ \mathcal{L}_J = \frac{1}{B} \sum_{i=1}^B \left\| \mathbf{F}_c(\mathbf{e}_i) - \mathbf{J}_\phi(\mathbf{e}_i) \nabla H_\theta(\mathbf{e}_i) \right\|^2, \\ \mathcal{L}_R = \frac{1}{B} \sum_{i=1}^B \left\| \mathbf{F}_d(\mathbf{e}_i) + \mathbf{R}_\psi(\mathbf{e}_i) \nabla H_\theta(\mathbf{e}_i) \right\|^2, \\ \mathcal{L}_{\text{Cons}} = \frac{1}{B} \sum_{i=1}^B \left(\nabla H_\theta(\mathbf{e}_i)^\top \mathbf{F}_c(\mathbf{e}_i) \right)^2, \\ \mathcal{L}_{\dot{H}} = \frac{1}{B} \sum_{i=1}^B \left(\nabla H_\theta(\mathbf{e}_i)^\top \dot{\mathbf{e}}_i^{\text{true}} - \nabla H_\theta(\mathbf{e}_i)^\top \mathbf{R}_\psi(\mathbf{e}_i) \nabla H_\theta(\mathbf{e}_i) \right)^2. \end{array} \right. \quad (31)$$

Each term enforces a distinct physical law: $\mathcal{L}_{\text{DynRes}}$ ensures dynamic consistency; \mathcal{L}_J and \mathcal{L}_R align learned and analytical conservative/non-conservative flows; $\mathcal{L}_{\text{Cons}}$ enforces energy invariance along conservative trajectories; and $\mathcal{L}_{\dot{H}}$ enforces the energy–rate identity (Eq. 29).

The synchronization energy is parameterized by a multilayer perceptron (MLP) $f_\theta : \mathbb{R}^n \rightarrow \mathbb{R}$ and anchored at the synchronization manifold to remove gauge freedom and ensure a strict local minimum:

$$H_\theta(\mathbf{e}) = f_\theta(\mathbf{e}) - \left(f_\theta(\mathbf{0}) + \nabla f_\theta(\mathbf{0})^\top \mathbf{e} \right) + \varepsilon \|\mathbf{e}\|_2^2, \quad (32)$$

so that $H_\theta(\mathbf{0}) = 0$ and $\nabla H_\theta(\mathbf{0}) = \mathbf{0}$.

Following Eq. (28) and the analytical decomposition in Eq. (20), we impose sparse interconnection and diagonal non-conservative structures for \mathbf{J}_ϕ and \mathbf{R}_ψ , respectively, while learning both via separate neural networks:

$$\mathbf{J}_\phi = \begin{pmatrix} 0 & * & ? & * & * \\ * & 0 & 0 & 0 & 0 \\ ? & 0 & 0 & 0 & 0 \\ * & 0 & 0 & 0 & 0 \\ * & 0 & 0 & 0 & 0 \end{pmatrix}, \quad \mathbf{R}_\psi = \begin{pmatrix} * & 0 & 0 & 0 & 0 \\ 0 & * & 0 & 0 & 0 \\ 0 & 0 & * & 0 & 0 \\ 0 & 0 & 0 & * & 0 \\ 0 & 0 & 0 & 0 & * \end{pmatrix},$$

This structure, inferred from \mathbf{F}_c and \mathbf{F}_d (Eq. (20)), reveals a sparse coupling pattern. We thus mask \mathbf{J}_ϕ and constrain \mathbf{R}_ψ to be diagonal, consistent with standard pH learning [39]. Because the sparsity pattern depends on the Hamiltonian gradient ∇H , we adopt a separable-gradient assumption, noting that many physical systems possess approximately separable energy functions [35, 57, 37]. Each component $\partial H/\partial e_i$ thus depends primarily on its own coordinate (and possibly a small subset), consistent with the weak cross-partials observed in \mathbf{F}_c and \mathbf{F}_d . Under this assumption, rows 2–5 of \mathbf{F}_c depend only on e_x , while $F_{c,x}$ depends on e_y, e_u , and e_ϕ (but not e_z), motivating a masked, skew-symmetric \mathbf{J}_ϕ ($\mathbf{J}_\phi^\top = -\mathbf{J}_\phi$). Inspection of \mathbf{F}_d further reveals primarily self-coupling (coordinate-wise damping) terms, motivating a diagonal parameterization of \mathbf{R}_ψ .

5.5. Training and Results

We train the pH-PINN by minimizing the total loss in Eq. (30). Supervision uses raw derivatives from the linearized error system (Eq. (6)) and from the coupled HR system (Eq. (2)). Each sample comprises the error state $\mathbf{e} \in \mathbb{R}^5$, its ground-truth derivative $\dot{\mathbf{e}}^{\text{true}}$, the full neuron states of both units (used only to build a short context vector $\mathbf{c} = (x_1, u_1, u_2, \phi_1)^\top \in \mathbb{R}^4$), and the analytical Hamiltonian and energy rate (H, \dot{H}) from Eqs. (23)–(24) for monitoring. We shuffle and split the data 80/20 into train/validation; no normalization is used. All networks consume the concatenated $[\mathbf{e}, \mathbf{c}]$ as input. Implementation details are summarized in Table 1, and the overall architecture is shown in Fig. 9.

Table 1: Implementation details of the pH-PINN blocks.

Block	Inputs (dim)	Architecture	Outputs
H_θ	$[\mathbf{e}, \mathbf{c}]$ (9)	width: 2048, depth: 1, activation: tanh , gauge anchoring at $\mathbf{e} = \mathbf{0}$, quadratic well $\varepsilon = 0.01$	scalar: H
J_ϕ	$[\mathbf{e}, \mathbf{c}]$ (9)	width: 32, depth: 4, activation: tanh , skew-symmetric J , sparse pattern	4 params: $[j_{12}, j_{13}, j_{14}, j_{15}]$
R_ψ	$[\mathbf{e}, \mathbf{c}]$ (9)	width: 2, depth: 2, activation: tanh , diagonal R	5 params: $\text{diag}(R_{11}, \dots, R_{55})$

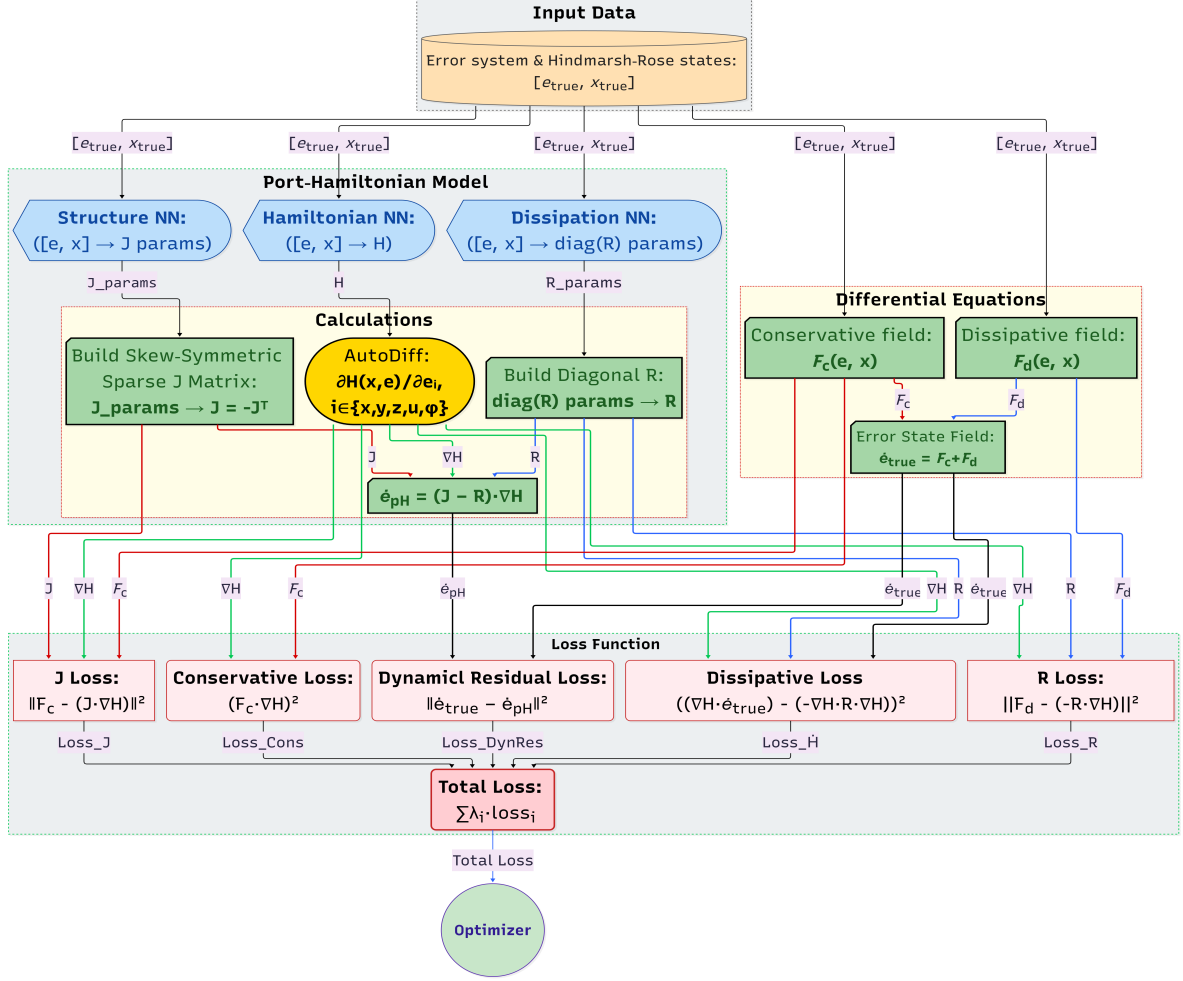


Figure 9: Schematic diagram of the proposed pH-PINN architecture.

We train using the AdamW optimizer [58] with a linear learning-rate decay from 1×10^{-3} to 1×10^{-5} during epochs 1–2000, and keep 1×10^{-5} thereafter until epoch 3000. We have total 200k samples and the batch size is 160k (full batch). All experiments are performed in JAX [50] (64-bit precision) using Equinox [59] modules and Optax optimizers; hyperparameters are tuned with Optuna [60]. Figure 10 reports the training and validation trajectories for the total loss together with the raw component losses from Eq. (30) (plotted before multiplying by their weights $\lambda_{\text{DynRes}}=0.5$, $\lambda_J=1$, $\lambda_R=1$, $\lambda_{\text{Cons}}=0.1$, $\lambda_{\dot{H}}=0.1$). For monitoring, we also track a Hamiltonian loss (against the analytical H) that does not contribute to optimization.

Two components, the conservative-invariance term $\mathcal{L}_{\text{Cons}}$ and the energy-rate consistency term $\mathcal{L}_{\dot{H}}$, start near zero, rise, and then descend alongside the others. This behaviour is expected as at initialization, the network can satisfy constraints involving ∇H_θ with a nearly flat Hamiltonian (so $\nabla H_\theta \approx 0$), yielding trivially small $\mathcal{L}_{\text{Cons}}$ and $\mathcal{L}_{\dot{H}}$. As the dynamics and non-conservative terms ($\mathcal{L}_{\text{DynRes}}$, \mathcal{L}_R) pull H_θ away from this degenerate solution, ∇H_θ becomes nonzero; these losses temporarily increase and then decrease as all constraints are reconciled. Overall, the total loss decreases smoothly with a small train-validation gap, and we keep the checkpoint with the best validation loss and stop training once the validation loss fails to improve beyond a small sensitivity threshold for several epochs.

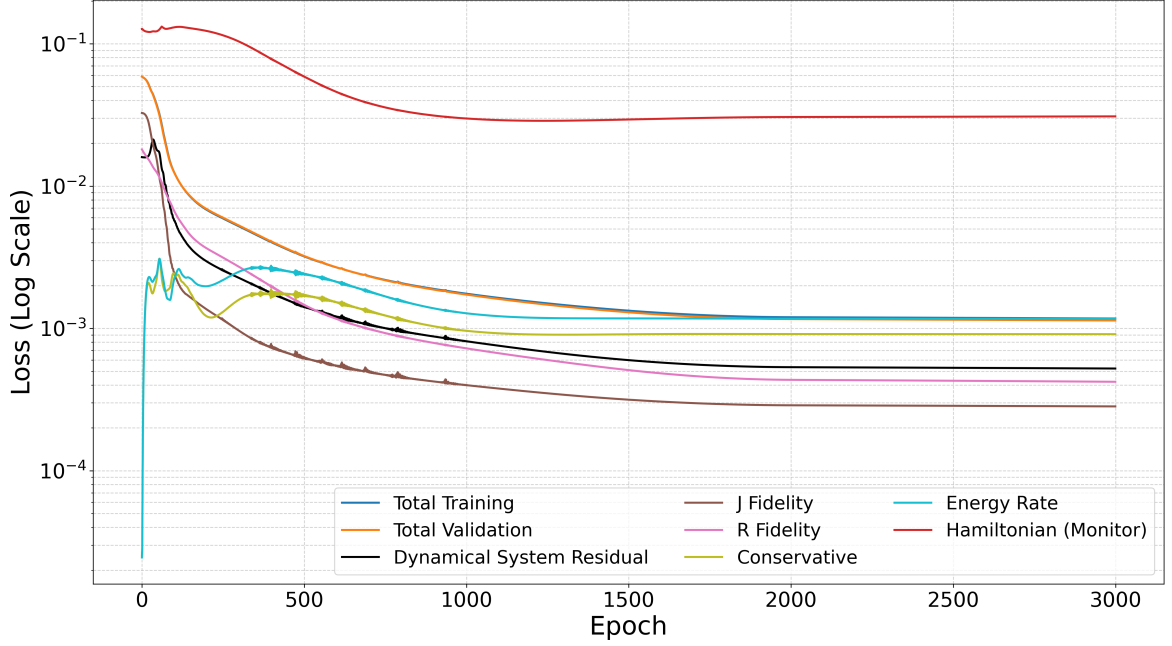


Figure 10: Training and validation loss curves over epochs. The convergence of the total loss, alongside the individual physics-based loss components, demonstrates successful model training and enforcement of physical constraints.

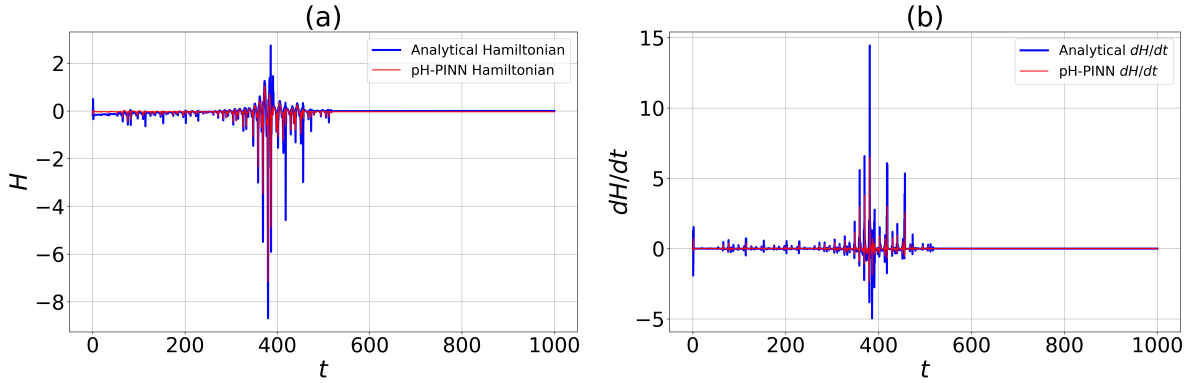


Figure 11: Comparison of analytically derived quantities and those discovered by the pH-PINN. Panel (a) shows Hamiltonian trajectories; panel (b) shows the time derivative of the Hamiltonian. The close agreement indicates the model has captured the underlying energy structure from data.

Figure 11 compares the learned and analytical energies. Panel (a) plots the pH-PINN Hamiltonian $H_\theta(\mathbf{e})$ against the analytical H from Eq. (23), while panel (b) compares the pH-PINN energy rate from Eq. (29), with the analytical \dot{H} in Eq. (24). The close alignment across trajectories shows that the model has recovered both the energy landscape and the \mathbf{J}/\mathbf{R} structure directly from data, without using the analytical energy expressions during training.

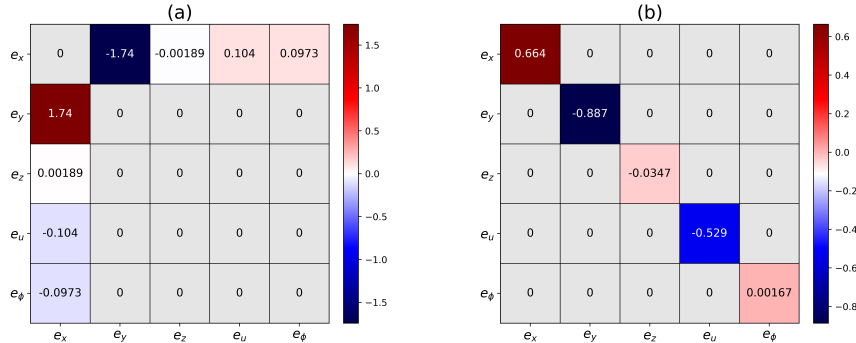


Figure 12: Time-averaged learned pH matrices. Panel (a): interconnection matrix $\langle \mathbf{J}_{\text{pred}} \rangle$; panel (b): symmetric matrix $\langle \mathbf{R}_{\text{pred}} \rangle$. The colormaps show the mean value of each entry over the entire validation dataset.

Figure 12 summarizes the learned pH factors. Panel (a) shows the time-averaged interconnection matrix $\langle \mathbf{J}_{\text{pred}} \rangle$, which is skew-symmetric and sparse. Entries related to e_z are relatively small compared to the others, consistent with the conservative field in Eq. (20), where no e_z dependence appears (even though, a priori, $\partial H / \partial e_z$ need not vanish). Eq. (20) further shows that the e_u and e_ϕ channels couple conservatively only through e_x ; accordingly, the network learns similar magnitudes for the $e_x \leftrightarrow e_u$ and $e_x \leftrightarrow e_\phi$ couplings. Panel (b) presents the symmetric matrix $\langle \mathbf{R}_{\text{pred}} \rangle$, which is diagonal as implied by separable-gradient assumption and Eq. (20).

6. Summary and conclusions

In this work, we established a rigorous and data-driven framework for chaotic synchronization in a five-dimensional Hindmarsh-Rose neuron model with electromagnetic induction and switchable memristive autapse. Our contributions are threefold.

(i) *Global asymptotic synchronization via Lyapunov analysis.* For two diffusively coupled neurons we derived the linearized error system and proved global asymptotic stability of the synchronization manifold \mathcal{M} using a quadratic Lyapunov function. By bounding the error dynamics and enforcing positivity of the leading principal minors (Sylvester’s criterion), we obtained verifiable sufficient conditions guaranteeing $\dot{V} \leq 0$ and, by Barbalat’s lemma, $\mathbf{e}(t) \rightarrow \mathbf{0}$ as $t \rightarrow \infty$. The analysis makes explicit how electrical coupling and intrinsic parameters jointly suppress transverse perturbations.

(ii) *Synchronization energy via Helmholtz decomposition.* We decomposed the error vector field into conservative and dissipative components and derived a closed-form synchronization Hamiltonian H and its energy-rate identity \dot{H} for the linearized error flow. This yields a quantitative measure of the energetic cost of synchrony and clarifies the respective roles of interconnection, damping, and the memristive offset in shaping energy exchange.

(iii) *Learning energetics with a port-Hamiltonian PINN.* We proposed a port-Hamiltonian physics-informed neural network (pH-PINN) that embeds the conservative/non-conservative structure into training through physically motivated losses. The model learns $(H_\theta, \mathbf{J}_\phi, \mathbf{R}_\psi)$ from data while enforcing skew-symmetry of \mathbf{J}_ϕ , diagonality of \mathbf{R}_ψ , and the energy balance $\dot{H}_\theta = -\nabla H_\theta^\top \mathbf{R}_\psi \nabla H_\theta$. Numerically, the learned Hamiltonian and energy rate closely match their analytical counterparts.

Direct simulations confirm complete synchronization and show monotone decay of the synchronization energy. Parameter sweeps across (k, ρ, m, g_e) reveal consistent trends between Lyapunov and Hamiltonian diagnostics: stronger electrical coupling accelerates synchronization, whereas excessive flux coupling can inject energy and delay convergence. Heatmaps of \dot{V} and \dot{H} agree across the parameter planes, supporting the equivalence of the two perspectives.

Our proof and learned structure are derived for the linearized error dynamics in a two-neuron setting with a separable-gradient prior. Extending the analysis to (i) nonidentical neurons and parameter mismatch, (ii) networks with arbitrary topology, (iii) stochastic forcing and measurement noise, and (iv) partial observability and latent-state identification are natural next steps. Methodologically, lifting the separability prior via adaptive masking, handling the piecewise memristive nonlinearity beyond linearization, and incorporating uncertainty quantification into the pH-PINN would broaden applicability. Finally, deploying the framework on experimental data and leveraging it for structure-preserving control design (*e.g.*, energy shaping and damping injection) are promising directions.

In summary, the paper provides (a) verifiable synchronization conditions for a biophysically enriched Hindmarsh–Rose model, (b) a closed-form synchronization energy and its energy–rate law, and (c) a principled learning architecture that discovers the same energetic structure directly from data. Together, these results bridge rigorous dynamical-systems analysis with physics-informed machine learning for nonlinear neuronal synchronization and offer a template for energy-aware modeling in broader classes of complex systems.

Acknowledgements

This work was funded by the Department of Data Science (DDS), Friedrich-Alexander-Universität Erlangen-Nürnberg, Germany, and the Deutsche Forschungsgemeinschaft (DFG, German Research Foundation) via the grant YA 764/1-1 to M.E.Y—Project No. 456989199.

Data availability

The codes developed and used to generate the data supporting the findings of this study are publicly accessible here [61].

References

- [1] E. Neustadter, K. Mathiak, B. I. Turetsky, EEG and MEG probes of schizophrenia pathophysiology, in: T. Abel, T. Nickl-Jockschat (Eds.), *The Neurobiology of Schizophrenia*, Academic Press, 2016, Ch. 13, pp. 213–236. doi:10.1016/B978-0-12-801829-3.00021-5.
- [2] K. Lehnertz, S. Bialonski, M.-T. Horstmann, D. Krug, A. Rothkegel, M. Staniek, T. Wagner, Synchronization phenomena in human epileptic brain networks, *Journal of Neuroscience Methods* 183 (1) (2009) 42–48. doi:10.1016/j.jneumeth.2009.05.015.
- [3] F. S. Borges, E. C. Gabrick, P. R. Protachevicz, G. S. V. Higa, E. L. Lameu, P. X. R. Rodriguez, M. S. A. Ferraz, J. Szezech, J. D., A. M. Batista, A. H. Kihara, Intermittency properties in a temporal lobe epilepsy model, *Epilepsy & Behavior* 139 (2023) 109072. doi:10.1016/j.yebeh.2022.109072.

- [4] P. R. Protachevich, F. S. Borges, E. L. Lameu, P. Ji, K. C. Iarosz, A. H. Kihara, I. L. Caldas, J. Szezech, Jose D., M. S. Baptista, E. E. N. Macau, C. G. Antonopoulos, A. M. Batista, J. Kurths, Bistable firing pattern in a neural network model, *Frontiers in Computational Neuroscience* 13 (2019) 19. doi:[10.3389/fncom.2019.00019](https://doi.org/10.3389/fncom.2019.00019).
- [5] S. Boccaletti, V. Latora, Y. Moreno, M. Chavez, D.-U. Hwang, Complex networks: Structure and dynamics, *Physics Reports* 424 (4-5) (2006) 175–308. doi:[10.1016/j.physrep.2005.10.009](https://doi.org/10.1016/j.physrep.2005.10.009).
- [6] G. V. Osipov, J. Kurths, C. Zhou, *Synchronization in Oscillatory Networks*, Springer Series in Synergetics, Springer Berlin Heidelberg, Berlin, Heidelberg, 2007. doi:[10.1007/978-3-540-71269-5](https://doi.org/10.1007/978-3-540-71269-5).
- [7] M. G. Rosenblum, A. S. Pikovsky, J. Kurths, Phase synchronization of chaotic oscillators, *Physical Review Letters* 76 (11) (1996) 1804–1807. doi:[10.1103/PhysRevLett.76.1804](https://doi.org/10.1103/PhysRevLett.76.1804).
- [8] A. S. Pikovsky, M. G. Rosenblum, J. Kurths, Synchronization in a population of globally coupled chaotic oscillators, *Europhysics Letters* 34 (3) (1996) 165–170. doi:[10.1209/epl/i1996-00433-3](https://doi.org/10.1209/epl/i1996-00433-3).
- [9] U. Parlitz, L. Junge, W. Lauterborn, L. Kocarev, Experimental observation of phase synchronization, *Physical Review E* 54 (2) (1996) 2115–2117. doi:[10.1103/PhysRevE.54.2115](https://doi.org/10.1103/PhysRevE.54.2115).
- [10] B. Pietras, A. Daffertshofer, Network dynamics of coupled oscillators and phase reduction techniques, *Physics Reports* 819 (2019) 1–105. doi:[10.1016/j.physrep.2019.06.001](https://doi.org/10.1016/j.physrep.2019.06.001).
- [11] J. Fell, N. Axmacher, The role of phase synchronization in memory processes, *Nature Reviews Neuroscience* 12 (2) (2011) 105–118. doi:[10.1038/nrn2979](https://doi.org/10.1038/nrn2979).
- [12] T. Dahms, J. Lehnert, E. Schöll, Cluster and group synchronization in delay-coupled networks, *Physical Review E* 86 (1) (2012) 016202. doi:[10.1103/PhysRevE.86.016202](https://doi.org/10.1103/PhysRevE.86.016202).
- [13] S. Jalan, R. Amritkar, Self-organized and driven phase synchronization in coupled maps, *Physical Review Letters* 90 (1) (2003) 014101. doi:[10.1103/PhysRevLett.90.014101](https://doi.org/10.1103/PhysRevLett.90.014101).
- [14] R. Amritkar, S. Jalan, Self-organized and driven phase synchronization in coupled map networks, *Physica A: Statistical Mechanics and its Applications* 321 (1-2) (2003) 220–225. doi:[10.1016/S0378-4371\(02\)01750-8](https://doi.org/10.1016/S0378-4371(02)01750-8).
- [15] H. D. Abarbanel, N. F. Rulkov, M. M. Sushchik, Generalized synchronization of chaos: The auxiliary system approach, *Physical Review E* 53 (5) (1996) 4528. doi:[10.1103/PhysRevE.53.4528](https://doi.org/10.1103/PhysRevE.53.4528).
- [16] Z. Zheng, G. Hu, Generalized synchronization versus phase synchronization, *Physical Review E* 62 (6) (2000) 7882. doi:[10.1103/PhysRevE.62.7882](https://doi.org/10.1103/PhysRevE.62.7882).
- [17] R. Femat, G. Solís-Perales, Synchronization of chaotic systems with different order, *Physical Review E* 65 (3) (2002) 036226. doi:[10.1103/PhysRevE.65.036226](https://doi.org/10.1103/PhysRevE.65.036226).
- [18] S. Bowong, P. V. E. McClintock, Adaptive synchronization between chaotic dynamical systems of different order, *Physics Letters A* 358 (2) (2006) 134–141. doi:[10.1016/j.physleta.2006.05.006](https://doi.org/10.1016/j.physleta.2006.05.006).

- [19] S. Bowong, Stability analysis for the synchronization of chaotic systems with different order: application to secure communications, *Physics Letters A* 326 (1-2) (2004) 102–113. [doi:10.1016/j.physleta.2004.04.004](https://doi.org/10.1016/j.physleta.2004.04.004).
- [20] J. Kobiolka, J. Habermann, M. E. Yamakou, Reduced-order adaptive synchronization in a chaotic neural network with parameter mismatch: a dynamical system versus machine learning approach, *Nonlinear Dynamics* 113 (10) (2025) 10989–11008. [doi:10.1007/s11071-024-10821-6](https://doi.org/10.1007/s11071-024-10821-6).
- [21] Q.-Y. Miao, J.-A. Fang, Y. Tang, A.-H. Dong, Increasing-order projective synchronization of chaotic systems with time delay, *Chinese Physics Letters* 26 (5) (2009) 050501. [doi:10.1088/0256-307X/26/5/050501](https://doi.org/10.1088/0256-307X/26/5/050501).
- [22] M. M. Al-sawalha, M. S. M. Noorani, Adaptive increasing-order synchronization and anti-synchronization of chaotic systems with uncertain parameters, *Chinese Physics Letters* 28 (11) (2011) 110507. [doi:10.1088/0256-307X/28/11/110507](https://doi.org/10.1088/0256-307X/28/11/110507).
- [23] L. M. Pecora, T. L. Carroll, Synchronization of chaotic systems, *Chaos: An Interdisciplinary Journal of Nonlinear Science* 25 (9) (2015). [doi:10.1063/1.4917383](https://doi.org/10.1063/1.4917383).
- [24] M. E. Yamakou, M. Desroches, S. Rodrigues, Synchronization in stdp-driven memristive neural networks with time-varying topology, *Journal of Biological Physics* 49 (4) (2023) 483–507. [doi:10.1007/s10867-023-09642-2](https://doi.org/10.1007/s10867-023-09642-2).
- [25] H. Fujisaka, T. Yamada, Stability theory of synchronized motion in coupled-oscillator systems, *Progress of Theoretical Physics* 69 (1) (1983) 32–47. [doi:10.1143/PTP.69.32](https://doi.org/10.1143/PTP.69.32).
- [26] E. M. Yamakou, E. M. Inack, F. M. Moukam Kakmeni, Ratcheting and energetic aspects of synchronization in coupled bursting neurons, *Nonlinear Dynamics* 83 (1-2) (2016) 541–554. [doi:10.1007/s11071-015-2346-0](https://doi.org/10.1007/s11071-015-2346-0).
- [27] Y. Tang, F. Qian, H. Gao, J. Kurths, Synchronization in complex networks and its application—a survey of recent advances and challenges, *Annual Reviews in Control* 38 (2) (2014) 184–198. [doi:10.1016/j.arcontrol.2014.09.003](https://doi.org/10.1016/j.arcontrol.2014.09.003).
- [28] S. Boccaletti, J. Kurths, G. Osipov, D. L. Valladares, C. Zhou, The synchronization of chaotic systems, *Physics Reports* 366 (1-2) (2002) 1–101. [doi:10.1016/S0370-1573\(02\)00137-0](https://doi.org/10.1016/S0370-1573(02)00137-0).
- [29] A. Arenas, A. D’iaz-Guilera, J. Kurths, Y. Moreno, C. Zhou, Synchronization in complex networks, *Physics Reports* 469 (3-4) (2008) 93–153. [doi:10.1016/j.physrep.2008.09.002](https://doi.org/10.1016/j.physrep.2008.09.002).
- [30] P. R. Protachevicz, M. Hansen, K. C. Iarosz, I. L. Caldas, A. M. Batista, J. Kurths, Emergence of neuronal synchronisation in coupled areas, *Frontiers in Computational Neuroscience* 15 (2021) 663408. [doi:10.3389/fncom.2021.663408](https://doi.org/10.3389/fncom.2021.663408).
- [31] F. S. Borges, P. R. Protachevicz, E. L. Lameu, R. C. Bonetti, K. C. Iarosz, I. L. Caldas, M. S. Baptista, A. M. Batista, Synchronised firing patterns in a random network of adaptive exponential integrate-and-fire neuron model, *Neural Networks* 90 (2017) 1–7. [doi:10.1016/j.neunet.2017.03.005](https://doi.org/10.1016/j.neunet.2017.03.005).

- [32] M. Raissi, P. Perdikaris, G. E. Karniadakis, Physics-informed neural networks: A deep learning framework for solving forward and inverse problems involving nonlinear partial differential equations, *Journal of Computational Physics* 378 (2019) 686–707. [doi:10.1016/j.jcp.2018.10.045](https://doi.org/10.1016/j.jcp.2018.10.045).
- [33] S. Wang, S. Sankaran, P. Perdikaris, Respecting causality is all you need for training physics-informed neural networks, *arXiv preprint arXiv:2203.07404* (2022). [doi:10.48550/arXiv.2203.07404](https://doi.org/10.48550/arXiv.2203.07404).
- [34] S. Cuomo, V. Schiano Di Cola, F. Giampaolo, G. Rozza, M. Raissi, F. Piccialli, Scientific machine learning through physics-informed neural networks: Where we are and what’s next, *Journal of Scientific Computing* 92 (3) (2022) 88. [doi:10.1007/s10915-022-01939-z](https://doi.org/10.1007/s10915-022-01939-z).
- [35] S. Greydanus, M. Dzamba, J. Yosinski, Hamiltonian neural networks, in: H. Wallach, H. Larochelle, A. Beygelzimer, F. d’Alch’e Buc, E. Fox, R. Garnett (Eds.), *Advances in Neural Information Processing Systems*, Vol. 32, Curran Associates, Inc., Vancouver, Canada, 2019, pp. 15353–15363. [arXiv:1906.01563](https://arxiv.org/abs/1906.01563).
- [36] M. Finzi, K. A. Wang, A. G. Wilson, Simplifying hamiltonian and lagrangian neural networks via explicit constraints, in: H. Larochelle, M. Ranzato, R. Hadsell, M. F. Balcan, H. Lin (Eds.), *Advances in Neural Information Processing Systems*, Vol. 33, Curran Associates, Inc., 2020, pp. 13880–13889. [arXiv:2010.13581](https://arxiv.org/abs/2010.13581).
- [37] Y. Chen, T. Matsubara, T. Yaguchi, Neural symplectic form: Learning hamiltonian equations on general coordinate systems, in: M. Ranzato, A. Beygelzimer, Y. Dauphin, P. S. Liang, J. Wortman Vaughan (Eds.), *Advances in Neural Information Processing Systems*, Vol. 34, Curran Associates, Inc., 2021, pp. 16659–16670, <https://proceedings.neurips.cc/paper/2021/hash/8b519f198dd26772e3e82874826b04aa-Abstract.html>.
- [38] A. van der Schaft, D. Jeltsema, *Port-Hamiltonian Systems Theory: An Introductory Overview*, Vol. 1 of *Foundations and Trends in Systems and Control*, Now Publishers Inc., Boston–Delft, 2014. [doi:10.1561/2600000002](https://doi.org/10.1561/2600000002).
- [39] S. Desai, M. Mattheakis, D. Sondak, P. Protopapas, S. Roberts, Port-hamiltonian neural networks for learning explicit time-dependent dynamical systems, *arXiv preprint arXiv:2107.08024*, journal ref: *Phys. Rev. E* 104, 034312 (2021) (2021). [doi:10.48550/arXiv.2107.08024](https://doi.org/10.48550/arXiv.2107.08024).
- [40] C. Neary, U. Topcu, Compositional learning of dynamical system models using port-hamiltonian neural networks, in: N. Matni, M. Morari, G. J. Pappas (Eds.), *Proceedings of The 5th Annual Learning for Dynamics and Control Conference (L4DC)*, Vol. 211 of *Proceedings of Machine Learning Research*, PMLR, Philadelphia, PA, USA, 2023, pp. 679–691. [arXiv:2212.00893](https://arxiv.org/abs/2212.00893).
- [41] S. Moradi, G. I. Beintema, N. Jaensson, R. Tóth, M. Schoukens, Port-hamiltonian neural networks with output error noise models *Preprint submitted to Automatica* (2025). [doi:10.48550/arXiv.2502.14432](https://doi.org/10.48550/arXiv.2502.14432).

- [42] L. Di Persio, M. Ehrhardt, Y. Outaleb, S. Rizzotto, Port-hamiltonian neural networks: From theory to simulation of interconnected stochastic systems, arXiv preprint arXiv:2509.06674 (2025). [doi:10.48550/arXiv.2509.06674](https://doi.org/10.48550/arXiv.2509.06674).
- [43] J.-P. Ortega, D. Yin, Learnability of linear port-hamiltonian systems, *Journal of Machine Learning Research* 25 (68) (2024) 1–56. [doi:10.48550/arXiv.2303.15779](https://doi.org/10.48550/arXiv.2303.15779).
- [44] J. L. Hindmarsh, R. M. Rose, A model of neuronal bursting using three coupled first order differential equations, *Proceedings of the Royal Society of London. Series B, Biological Sciences* 221 (1222) (1984) 87–102. [doi:10.1098/rspb.1984.0024](https://doi.org/10.1098/rspb.1984.0024).
- [45] A. I. Selverston, M. I. Rabinovich, H. D. I. Abarbanel, R. Elson, A. Szucs, R. D. Pinto, R. Huerta, P. Varona, Reliable circuits from irregular neurons: a dynamical approach to understanding central pattern generators, *Journal of Physiology-Paris* 94 (5-6) (2000) 357–374. [doi:10.1016/S0928-4257\(00\)01101-3](https://doi.org/10.1016/S0928-4257(00)01101-3).
- [46] M. Lv, C. Wang, G. Ren, J. Ma, X. Song, Model of electrical activity in a neuron under magnetic flow effect, *Nonlinear Dynamics* 85 (3) (2016) 1479–1490. [doi:10.1007/s11071-016-2773-6](https://doi.org/10.1007/s11071-016-2773-6).
- [47] M. E. Yamakou, Chaotic synchronization of memristive neurons: Lyapunov function versus hamilton function, *Nonlinear Dynamics* 101 (1) (2020) 487–500. [doi:10.1007/s11071-020-05715-2](https://doi.org/10.1007/s11071-020-05715-2).
- [48] J. Zhang, Z. Li, Switchable memristor-based hindmarsh–rose neuron under electromagnetic radiation, *Nonlinear Dynamics* 112 (8) (2024) 6647–6662. [doi:10.1007/s11071-024-09399-w](https://doi.org/10.1007/s11071-024-09399-w).
- [49] J. Ma, Y. Wang, C. Wang, Y. Xu, G. Ren, Mode selection in electrical activities of myocardial cell exposed to electromagnetic radiation, *Chaos, Solitons & Fractals* 99 (2017) 219–225. [doi:10.1016/j.chaos.2017.04.016](https://doi.org/10.1016/j.chaos.2017.04.016).
- [50] J. Bradbury, R. Frostig, P. Hawkins, M. J. Johnson, C. Leary, D. Maclaurin, S. Wanderman-Milne, JAX: Composable transformations of python+numpy programs, <https://github.com/google/jax> (2018).
- [51] P. Kidger, Diffrax, <https://github.com/patrick-kidger/diffrax>, gitHub repository.
- [52] C. Tsitouras, Runge–kutta pairs of order 5(4) satisfying only the first column simplifying assumption, *Computers & Mathematics with Applications* 62 (2) (2011) 770–775. [doi:10.1016/j.camwa.2011.06.002](https://doi.org/10.1016/j.camwa.2011.06.002).
- [53] N. N. Krasovskii, *Stability of Motion: Applications of Lyapunov’s Second Method to Differential Systems and Equations with Delay*, Stanford University Press, Stanford, CA, 1963, english translation of the 1959 Russian edition.
- [54] D. H. Kobe, Helmholtz’s theorem revisited, *American Journal of Physics* 54 (6) (1986) 552–554. [doi:10.1119/1.14562](https://doi.org/10.1119/1.14562).
- [55] C.-N. Wang, Y. Wang, J. Ma, Calculation of hamilton energy function of dynamical system by using helmholtz theorem, *Acta Physica Sinica* 65 (24) (2016) 240501. [doi:10.7498/aps.65.240501](https://doi.org/10.7498/aps.65.240501).

- [56] J. Ma, F. Wu, W. Jin, P. Zhou, T. Hayat, Calculation of hamilton energy and control of dynamical systems with different types of attractors, *Chaos: An Interdisciplinary Journal of Nonlinear Science* 27 (5) (2017). doi:10.1063/1.4983469.
- [57] Y. D. Zhong, B. Dey, A. Chakraborty, Symplectic ODE-net: Learning hamiltonian dynamics with control, arXiv (sep 2019). doi:10.48550/arXiv.1909.12077.
- [58] I. Loshchilov, F. Hutter, Decoupled weight decay regularization, in: International Conference on Learning Representations, New Orleans, LA, USA, 2019. doi:10.48550/arXiv.1711.05101.
- [59] P. Kidger, Equinox: Neural networks in JAX via functional programming, <https://github.com/patrick-kidger/equinox> (2021).
- [60] T. Akiba, S. Sano, T. Yanase, T. Ohta, M. Koyama, Optuna: A next-generation hyperparameter optimization framework, in: Proceedings of the 25th ACM SIGKDD International Conference on Knowledge Discovery & Data Mining, KDD '19, Association for Computing Machinery, Anchorage, AK, USA, 2019, pp. 2623–2631. doi:10.1145/3292500.3330701.
- [61] <https://github.com/Behnam2553/port-Hamiltonian-PINN-and-HR-neuron.git> (2025).